Intermediate spectral statistics of rational triangular quantum billiards

Črt Lozej [1] and Eugene Bogomolny [2]
[1] *Max Planck Institute for the Physics of Complex Systems, 01187 Dresden, Germany*
[2] *Université Paris-Saclay, CNRS, LPTMS, 91405 Orsay, France*

(Received 19 June 2024; accepted 15 July 2024; published 22 August 2024)

Triangular billiards whose angles are rational multiples of π are one of the simplest examples of pseudo-integrable models with intriguing classical and quantum properties. We perform an extensive numerical study of spectral statistics of eight quantized rational triangles, six belonging to the family of right-angled Veech triangles and two obtuse rational triangles. Large spectral samples of up to one million energy levels were calculated for each triangle, which permits one to determine their spectral statistics with great accuracy. It is demonstrated that they are of the intermediate type, sharing some features with chaotic systems, like level repulsion, and some with integrable systems, like exponential tails of the level spacing distributions. Another distinctive feature of intermediate spectral statistics is a finite value of the level compressibility. The short-range statistics such as the level spacing distributions, and long-range statistics such as the number variance and spectral form factors were analyzed in detail. An excellent agreement between the numerical data and the model of gamma distributions is revealed.

DOI: 10.1103/PhysRevE.110.024213

I. INTRODUCTION

The study of quantum chaos [1,2] relates concepts of classical ergodic theory to quantum systems. There are two main conjectures that connect spectral statistical properties of quantum systems with classical dynamical features: (1) The quantum chaos or Bohigas-Giannoni-Schmit conjecture [3,4] states that generic chaotic quantum systems should have spectral statistics (or quantum statistical properties in general) that are described by an appropriate ensemble of random matrix theory (RMT). The appropriate ensemble is determined solely by unitary and antiunitary (say, time-reversal) symmetries of the system. (2) The Berry-Tabor conjecture [5] states that generic integrable systems are described by the Poisson statistics. Both have been tested and corroborated by an extensive number of examples and form the foundation of quantum chaos.

However, they do not cover all possible types of dynamical systems. In this paper, we focus on the so-called *pseudo-integrable* models [6]. For simplicity, let us consider only two-dimensional Hamiltonian systems. Classical integrable systems of this kind are characterized by the fact that a typical trajectory will belong to a torus (i.e., a two-dimensional surface of genus 1). In contrast, the trajectories of chaotic systems will cover the entire three-dimensional surface of constant energy. In pseudo-integrable systems, the trajectories will spread over two-dimensional surfaces of genus higher than 1, which explains their name. Plane polygonal billiards whose internal angles are rational fractions of π,

$$\varphi_i = \frac{n_j}{m_j}\pi, \tag{1}$$

with coprime integers n_j and m_j are a characteristic example of such a system. It is proven [7] that the genus of the surface in this case is given by

$$g = 1 + \frac{M}{2}\sum_j \frac{n_j - 1}{m_j}, \tag{2}$$

where M is the least common multiple of all the denominators m_j.

In spite of their apparent simplicity, the study of polygonal billiards is notoriously challenging (see [8,9] and references therein), and analytical results are usually limited to specific cases. The mechanisms of defocusing [10] and focusing-defocusing [11,12] that result in chaotic dynamics in billiards are well known and require curved boundaries. Because of this, polygonal billiards are strictly nonchaotic and the well-developed methods for chaotic systems of ergodic theory do not apply. For instance, even the general periodic orbit structure and the existence of periodic orbits (see, e.g., Ref. [13] for triangles) are hard to prove. The exception are the Veech polygons [14], which possess the so-called lattice property, and consequently the properties of the periodic orbits are known.

Triangular billiards have a rich landscape of distinct dynamical regimes in their own right. Based on numerical evidence, generic triangles (all angles have irrational ratios with π) are believed to be strongly mixing [15]. On the other hand, irrational triangles with one rational angle, such as right triangles, have weaker ergodic properties [16–18],

and the most recent numerical evidence suggests they are not ergodic in the Lebesgue measure [19–21]. The quantum triangular billiards of these classes have been explored in [22]. Based on relations (1) and (2) rational triangles belong to the pseudo-integrable regime. Specifically, the list of known Veech triangles is given in Ref. [23]. In particular, the family of Veech right triangles with one of the angles equal to π divided by an integer will be of interest for this paper.

The knowledge of quantum properties of pseudo-integrable billiards is fragmentary and includes mainly numerical calculations for billiards of simple shape: rhombus, right triangles, rectangular billiard with a barrier, etc. [24–30]. The only quantity that is accessible to analytical derivations is the *spectral compressibility* χ, which determines the growth of the variance [31] of the of number of levels in an interval of length L,

$$\langle (N(L)-L)^2 \rangle \underset{L\to\infty}{\sim} \chi L, \tag{3}$$

where $N(L)$ is normalized such that its mean value equals L and the angled brackets denote an averaging over a small energy window. The compressibility distinguishes between chaotic $\chi = 0$ and integrable models $\chi = 1$. The calculation of the compressibility is done by the summation over classical periodic orbits in the diagonal approximation [31]. In the particular case of the above-mentioned Veech right triangles with angles π/m, the compressibility is given by [32]

$$\chi = \frac{m+\epsilon(m)}{3(m-2)}, \tag{4}$$

which depends on the factors of m such that $\epsilon(m) = 0$ for odd m, $\epsilon(m) = 2$ for even m but $m \not\equiv 0 \mod 3$, and $\epsilon(m) = 6$ for $m \equiv 0 \mod 6$. Similarly, analytical results in barrier billiards show $\chi = 1/2$ regardless of the barrier height [33,34]. As we see, the spectral properties of pseudo-integrable systems can subtly depend on structural details. The fact that for these models $0 < \chi < 1$ is indicative that spectral statistics of such billiards are different from those of both chaotic and integrable models, but share similarities with both. This is why they are referred to as *intermediate spectral statistics*. The best-known example is the semi-Poisson statistics [28], which may be obtained by taking only every second level of a Poissonian spectrum. Incidentally, this corresponds to $\chi = 1/2$.

Numerical observations of intermediate spectral statistics have established the following properties: (1) level repulsion at small distances, as in the standard random matrix ensembles; (2) exponential tails of nearest-neighbor spacing distributions, as in the Poissonian case; (3) nontrivial value of the spectral compressibility; and (4) multifractal dimensions of eigenfunctions [35,36]. This type of statistics was first observed at the metal-insulator transition point in the Anderson model [37,38] and in a variety of other dynamical systems including the already mentioned billiards, but also in neutrino billiards [39], quantum maps [40], short-range plasma models [28,41], and models of structured random matrices [42,43].

The principal results of the paper are the following: (1) the spectral statistics of rational triangular quantum billiards are of the intermediate type and (2) the correlation functions are well described by simple gamma distribution formulas. These conclusions are based on numerical computations of large spectra of up to 1 million eigenenergies of eight triangles, namely, six Veech right triangles and two non-Veech obtuse triangles, with subsequent analysis of nearest-neighbor and higher-order level spacing distributions, the number variance, the spectral form factor, and level compressibility for all these models.

The plan of the paper is the follows. In Sec. II the quantum billiard problem, the geometries of the triangular billiards, and the spectral statistics considered in this study are defined. In Sec. III the numerical results are presented and analyzed. In Sec. IV the conclusions are presented and discussed. Appendix A offers a heuristic explanation for the success of the gamma distributions by using a toy model. In Appendix B some more complicated two-parameter fitting distributions are presented.

II. DEFINITIONS

This section gives all the relevant definitions of the dynamical system, quantities, and their relationships considered in this paper, and introduces notation.

A. Quantum billiards

Dynamical billiards are archetypical models of both classical and quantum chaos. In a two-dimensional quantum billiard problem, one considers a quantum particle trapped inside a region $\mathcal{B} \subset \mathbb{R}^2$ known as the billiard table. The eigenfuncitons $\psi_n(x)$ are given by the solutions of the Helmholtz equation

$$\left(\nabla^2 + k_n^2\right)\psi_n(x) = 0 \tag{5}$$

with certain boundary conditions (BCs). In this study, only triangular regions and Dirichlet BCs are considered. In means that $\psi_n|_{\partial\mathcal{B}} = 0$, with eigenenergies $E_n = k_n^2$, where k_n is the wave number of the nth eigenstate.

The very efficient scaling method, devised by Vergini and Saraceno [44,45] and extensively studied by Barnett [46], with a corner adapted Fourier-Bessel basis [47], allows us to compute very large spectra of the order of 10^6 states. The implementation is available as part of [48] and is the same as used in [22].

The spectral staircase function counts the number of eigenstates (or modes) up to some energy $N(E) := \#\{n|E_n < E\}$. The asymptotic mean of the spectral staircase for billiards is given by the well-known generalized Weyl's law [49]

$$N_{\text{Weyl}}(E) = (\mathcal{A}E - \mathcal{L}\sqrt{E})/4\pi + \sum_i \frac{\pi^2 - {\varphi_i}^2}{24\pi\varphi_i}, \tag{6}$$

where $\mathcal{A}$ is the area of the billiard and $\mathcal{L}$ the circumference and φ_i are the internal angles. To compare the universal statistical fluctuations for different billiards, it is convenient to unfold the spectra. This is done by inserting the numerically computed billiard spectrum into Weyl's formula $e_n := N_{\text{Weyl}}(E_n)$. The resulting unfolded spectrum e_n has a uniform mean level density equal to one.

B. Geometry

In this study, the spectra of eight triangular quantum billiards with all angles having rational ratios with π are considered. Of these, six were taken from the family of Veech right triangles, with angles $(\frac{\pi}{m}, \frac{(m-2)\pi}{2m}, \frac{\pi}{2})$ for $m \geqslant 4$. The triangles from this group are labeled as V_m. Only six triangles $V_5, V_7, V_8, V_9, V_{10}, V_{18}$ are investigated. The triangles V_4 and V_6 are integrable and thus not interesting for this study.

As explained in the introduction, the periodic orbit structure of the Veech triangles is known, and therefore semiclassical techniques may be used to gain analytical insight into their spectral statistics, namely, Eq. (4) for the level compressibility.

To expand the scope of our study to more general rational triangles two non-Veech obtuse triangles with angles $(\frac{2\pi}{15}, \frac{4\pi}{15}, \frac{3\pi}{5})$ and $(\frac{2\pi}{25}, \frac{6\pi}{25}, \frac{3\pi}{5})$ are also considered. These triangles are labeled, respectively, by T_1 and T_2. In these cases, the classical periodic orbit structure is not known. The height, measured from the bottom side of the triangles, is fixed to $h = 1$ in all cases. As an illustration, Fig. 1 shows typical eigenstates of the triangles V_5 and T_2 as well as a superscar state of V_5. For more information about superscars the reader is referred to Refs. [35,36].

C. Level spacings

The distributions of level spacings are the most commonly considered spectral statistics. Let $P_n(s)$ be the nth nearest-neighbor spacing distribution, that is, the probability density of the energy distances s between two levels that have n levels between them. For $n = 0$ this is the nearest-neighbor level spacing distribution, which is the most studied. The distributions follow the normalization conditions

$$\int_0^\infty P_n(s)\,ds = 1, \quad \int_0^\infty sP_n(s)\,ds = 1 + n. \tag{7}$$

There are several well-supported conjectures that relate level spacing distributions of quantum mechanical dynamical systems to random matrix models. The Bohigas-Giannoni-Schmit conjecture [3,4] states the spectral statistics of chaotic models will follow the statistics of Gaussian random matrices, and the Berry-Tabor conjecture [50] states that integrable models follow Poissonian statistics. In chaotic systems with time-reversal symmetry, the Wigner surmise gives an excellent approximation for the nearest-neighbor spacing distribution

$$P_W(s) = \frac{\pi}{2} s \exp\left(-\frac{\pi}{4}s^2\right). \tag{8}$$

Higher-order spacing surmises are given in [51]. In the integrable (Poissonian) case the distribution is exponential,

$$P_I(s) = \exp(-s). \tag{9}$$

The behavior of $P(s)$ as $s \to 0$ is a notable and distinguishing feature. We see $P(s) \propto s^\beta$, for small s, with $\beta = 1$ in the chaotic and $\beta = 0$ in the integrable case. The energy levels in the chaotic case tend to form a gap (are repulsed) between each other, induced by correlations in the energy spectrum. In the integrable case, the levels are uncorrelated and have no level repulsion. The exponent β is called the level repulsion exponent. However, interesting dynamical regimes between chaos and integrability also exist, for instance, dynamical localization (see, for instance, [52–55]). These can be modeled by using the Brody distribution [56], which interpolates the two regimes

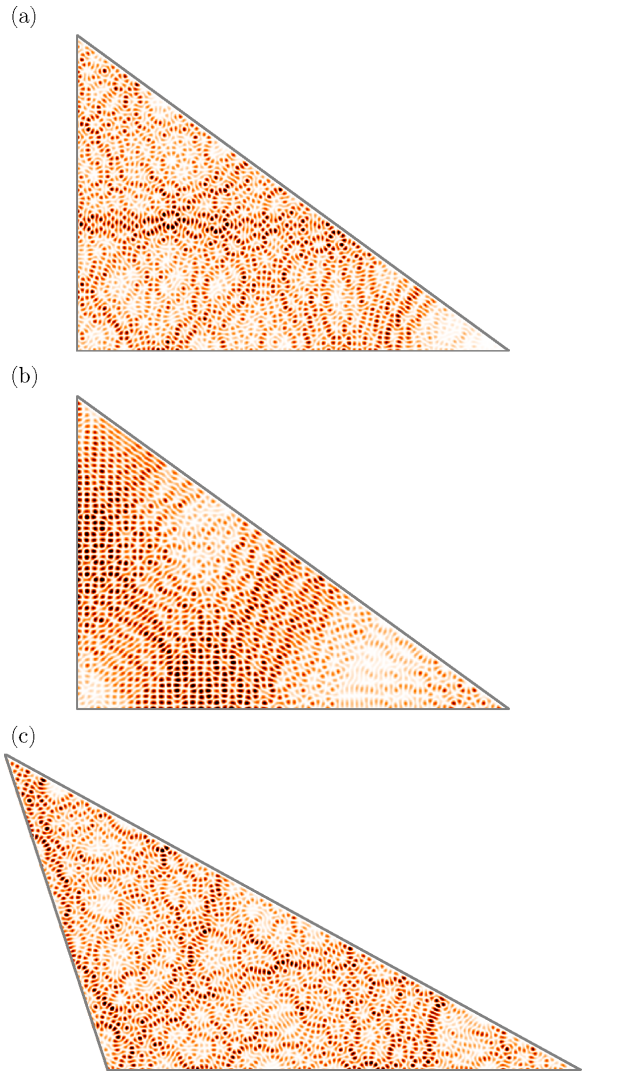

FIG. 1. Examples of eigenstates of rational triangular billiards. We show the probability distribution $|\psi_n|^2$ for (a) the Veech triangle V_5, generic eigenstate $n = 3342$ at $k = 250.0099$, (b) superscar eigenstate $n = 2430$ at $k = 213.6317$, and (c) obtuse triangle T_2, generic eigenstate $n = 3624$ at $k = 250.0095$.

$$P_B(s) = as^\beta \exp(-bs^{\beta+1}), \tag{10}$$

where the normalization constants (7) with $n = 0$ are given by $a = (\beta + 1)b$, and $b = [\Gamma(\frac{\beta+2}{\beta+1})]^{\beta+1}$, where $\Gamma(x)$ is the gamma function. We see that both the level repulsion and the tail of the distribution change as we interpolate from $\beta = 0$ to $\beta = 1$. However, as we will later confirm with the numerics, the level spacings of the rational triangles have slightly different characteristics, namely, (1) level repulsion at small s and (2) a purely exponential tail at large s. Because they share characteristics of both chaotic and integrable spectra, they are known as *intermediate spectral statistics*. The best-known

example is the semi-Poisson distribution,

$$P_{SP}(s) = 4s\exp(-2s). \tag{11}$$

The main model for the level spacings of the rational triangles will be a normalized version of the family of gamma distributions. The probability density function for the nth level spacing is given by

$$P_n(s) = a_n s^{\gamma_n}\exp(-b_n s), \tag{12}$$

where a_n and b_n are obtained from the normalization conditions (7),

$$a_n = \frac{1}{\Gamma(\gamma_n+1)}\left(\frac{\gamma_n+1}{n+1}\right)^{\gamma_n+1}, \qquad b_n = \frac{\gamma_n+1}{n+1}. \tag{13}$$

The parameter γ_n will depend on the order of the level spacing n. It appears that a linear dependence

$$\gamma_n = pn + \gamma_0, \tag{14}$$

where γ_0 and p are fitting parameters consistent with the numerical data. Setting $\gamma_0 = 0$ and $p = 1$ corresponds to the Poisson model and $\gamma_0 = 1$ and $p = 2$ to semi-Poisson. The gamma model is not new and has been used previously to describe spectra of structured random matrices [43], where the parameters are related to the "zero modes" of the matrices; that is, the number of parameters whose variation does not remove the eigenvalue degeneracy. In Appendix A a toy model that offers a heuristic explanation for the success of the gamma model is presented.

D. Two-point correlations

The two-point correlation function $R_2(s)$ is the probability that two levels are separated by the distance s. Since there can be any number of levels in between, it is equal to the sum over all orders of the spacing distributions

$$R_2(s) = \sum_{n=0}^{\infty} P_n(s). \tag{15}$$

Many interesting spectral statistics are related to the two-point correlation function. In this paper we will focus on the number variance and the spectral form factor. The number variance is the local variance of the number of levels in an interval of length L, given by

$$\Sigma^2(L,e) := \langle (N(L,x)-L)^2\rangle_{e,w} \quad L>0, \tag{16}$$

where $N(L,x) = N(x+L/2) - N(x-L/2)$ is the number of unfolded energy levels e_n in the interval $[x-L/2,\ x+L/2]$. The brackets $\langle\cdots\rangle_{e,w}$ denote a local average around the central energy e and window width w, so that $x\in[e-w/2,\ e+w/2]$. The number variance is related to the two-point correlations via the integral,

$$\Sigma^2(L) = L - 2\int_0^L (L-s)[1-R_2(s)]\,ds. \tag{17}$$

Particular interesting is the long-range limit of the number variance

$$\Sigma^2(L) \underset{L\to\infty}{\sim} \chi L, \tag{18}$$

where the proportionality coefficient χ is called the *level compressibility*. Therefore, the compressibility can be defined as

$$\chi = \lim_{L\to\infty}\frac{\Sigma^2(L)}{L}. \tag{19}$$

This yields $\chi = 0$ for the Gaussian ensembles of random matrices and $\chi = 1$ in the Poisson case. For the intermediate spectral statistics, it is argued [37,38] that $0<\chi<1$. Since the number variance can be expressed from the two-point correlation function, one may use the relation (15), the model assumptions (12), and (14) to compute the spectral compressibility for the gamma model (see Ref. [43] for a complete derivation). The end result is simply

$$\chi = \frac{1}{p}. \tag{20}$$

The spectral form factor (SFF) is the Fourier transform of the two-point correlation function

$$K(t) = \int_{-\infty}^{\infty} R_2(s)e^{2\pi i t s}\,ds. \tag{21}$$

The compressibility may also be expressed as the limit

$$\chi = \lim_{t\to 0} K(t). \tag{22}$$

The form factor can be expressed formally through the spectrum as follows:

$$K(t) = \left\langle \left| \sum_n^N \exp(2\pi i e_n t)\right|^2\right\rangle, \tag{23}$$

where the sum goes over the unfolded energy levels, and $\langle\cdots\rangle$ represents an average over an ensemble of similar systems or a moving time average as discussed below at the end of the section. The form factor is a very sensitive measure of quantum chaos due to its very distinct behavior in different dynamical regimes. In the Poissonian (integrable) case $K(t) = 1$. In the chaotic (GOE) case it is given by the formula [57]

$$K_{\mathrm{GOE}}(t) = \begin{cases} 2t - t\ln(2t+1) & t<1 \\ 2 - t\ln\left(\frac{2t+1}{2t-1}\right) & t>1 \end{cases}. \tag{24}$$

From this expression it follows that $K_{\mathrm{GOE}}(t\to 0) = 0$.

In the case of intermediate spectral statistics, we may expect $K(t)$ will approach a nontrivial value $0<\chi<1$ as $t\to 0$. Following Ref. [43], the Fourier transform (21) may be evaluated by introducing the Laplace transform

$$K(t) = 1 + \mathrm{Re}\, g(2\pi i t), \tag{25}$$

where g is defined as

$$g(\tau) = \sum_{n=0}^{\infty} g_n(\tau), \tag{26}$$

that is, the Laplace transform of the sum (15) and

$$g_n(\tau) = \int_0^{\infty} P_n(s)e^{-\tau s}\,ds. \tag{27}$$

Using the gamma distributions (12) and the linear dependence (14) a technical derivation (see Ref. [43])

yields the expression

$$g(\tau) = \frac{\left(1+\frac{\tau}{p}\right)^{p-\gamma_0-1}}{\left(1+\frac{\tau}{p}\right)^{p}-1} \exp\left(-\frac{\tau(p-\gamma_0-1)}{p+\tau}\right), \qquad (28)$$

which can be used to evaluate (25). Taking the limit $t \to 0$ produces $\chi = 1/p$, which is, of course, consistent with the derivation from the number variance.

Finally, we shall make a few comments regarding the numerical evaluation of the spectral form factor. It is known the SFF is not a self-averaging quantity [58] and exhibits erratic fluctuations with time. This means a separate averaging must be performed, represented by $\langle\cdots\rangle$. This is commonly an average over different realizations when considering random matrices or disordered systems. For clean single-body systems such as billiards, instead it is necessary to perform a moving time average to smooth out the fluctuations [59,60]. The procedure is exactly as used in previous papers [22,55], to which we refer the reader for further details. Furthermore, when considering the $t \to 0$ limit in definitions such as (22) it is implicitly assumed the limit $N \to \infty$ is taken first, i.e., the whole infinite spectrum is considered, which is not possible in the numerics. Therefore, the limits are necessarily inverted, and formally the form factor diverges at $t = 0$. This can be seen, e.g., by taking Eq. (23) and considering the limit $\lim_{N\to\infty} K(0) = N \to \infty$. This drawback can be avoided by decomposing the form factor into the connected and disconnected parts (stemming from the connected and disconnected two-point correlation functions). The disconnected part is given by the diagonal terms from Eq. (23) and depends solely on the density of states (see Ref. [61] for more details). Considering only the connected part of the spectral form factor by subtracting the disconnected part eliminates the divergences in the numerical calculations. Hence, only the connected parts of the spectral form factors are shown in the numerical results.

III. NUMERICAL RESULTS

The spectral samples were produced by the scaling method as implemented in [48]. The scaling method computes the states in some small, finite spectral interval. The final spectral sample is a composite of many small overlapping spectral samples, where we try to identify which of the levels in the overlap interval belong to the same eigenstates. Because of the finite precision and numerical errors in the computation of the individual levels this is not always possible, and some levels are missed, while some may be counted twice. To omit the nonuniversal aspects of the low-lying eigenstates, we start collecting the levels from the 10 000th onward. The samples for the Veech triangles contain 10^6 consecutive levels, the exception being V_{18}, where we start with the 10^5-th level and gather only 8×10^5 levels. The remaining two samples contain 6×10^5 levels for T_1 and 10^6 levels for T_2. The number of mistakes is less than 100 in all cases, which should have no significant impact on the results.

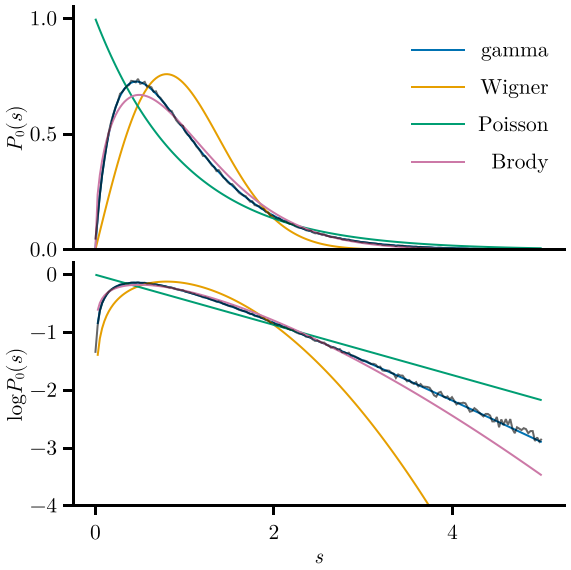

FIG. 2. Nearest-neighbor level spacing distributions in triangle V_5. The numerical results are shown in gray. The colored curves show the model predictions.

A. Level spacings

We will start with examining the level spacing distributions. In Fig. 2 we show the nearest-neighbor level spacings for the Veech triangle V_5 compared to the analytical models in the linear (top) and log-linear scales. As expected, we observe intermediate spectral statistics, as neither the Poissonian (9) nor Wigner-Dyson (8) models fit the data. The Brody distribution (10) is better and captures the level repulsion, but clearly misses the top and the tail of the distribution. The gamma distribution fit is clearly the best and fits the data nearly perfectly. It is evident from the log-linear plot that the tail of the distribution is indeed exponential. In Fig. 3 we show the level spacings for order up to $n = 7$ in the same triangle V_5. We compare the data with the best fitting gamma distribution for each order. Again, the distributions fit the data

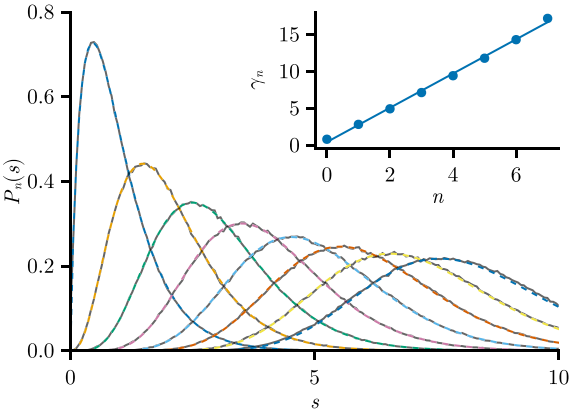

FIG. 3. Level spacing distributions up to order $n = 7$ for the triangle V_5. The numerical data are shown in gray. The dashed colored curves show the fitted gamma distributions (12). The insert shows the linear dependence of the fitted parameters γ_n together with the best fitting line (14).

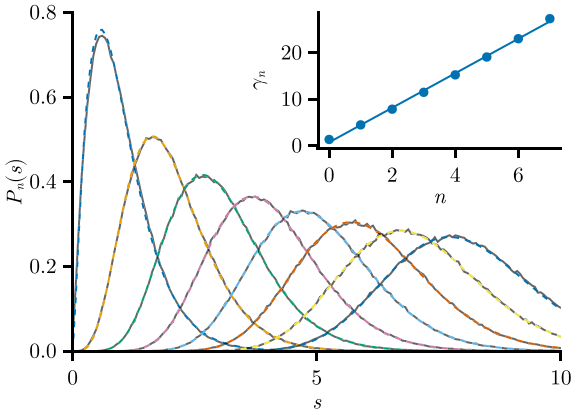

FIG. 4. Same as Fig. 3, but for the obtuse triangle T_1.

extremely well. The insert shows the values of the fitted γ_n as a function of n. A linear dependence of type (14) with parameters $\gamma_0 = 0.75$ and $p = 2.91$ approximates the data well. In Fig. 4 the same quantities for the rational triangle T_1 are shown. The fits are of similar quality with $\gamma_0 = 1.14$ and $p = 4.62$. We repeat the procedure (the best fitting γ_n for $n \leqslant 4$ is given in Table I) for the other triangles, and then obtain values for γ_0 and p from the linear fits. In Fig. 5 we show $P_n(s)$ up to $n = 4$ in the log-linear scale, for all the triangles considered in this study. Instead of fitting the gamma distribution for each order separately, we use the parameters γ_0 and p extracted from the previous step and use the linear relationship to determine the next γ_n in the sequence. Comparing the data to the model curves, we see very good agreement between the model and the numerics. The largest deviations occur in the tails of nearest-neighbor spacings, $P_0(s)$, since the fitted linear sequence sometimes slightly underestimates the value of γ_0 compared to the best fitting parameter. These small deviations would hardly be visible in the linear plot, and we

TABLE I. The best fitting parameters γ_n for the gamma distributions describing the level spacing distributions $P_n(s)$ up to $n = 4$.

Label	γ_0	γ_1	γ_2	γ_3	γ_4
V_5	0.84	2.86	4.97	7.17	9.46
V_7	1.12	3.66	6.41	9.31	12.35
V_8	0.82	3.66	6.41	6.96	9.10
V_9	1.29	4.20	7.38	10.74	14.26
V_{10}	0.92	3.10	5.47	7.93	10.52
V_{18}	1.27	4.07	7.07	10.25	13.53
T_1	1.36	4.50	7.88	11.51	15.27
T_2	1.69	5.64	9.95	14.52	19.18

may conclude the model is a very good approximation despite its simplicity. Some more complicated two-parameter extensions for fitting distributions are explored in Appendix B. It is interesting that the gamma model works equally well for the Veech triangles and the other two rational triangles T_1 and T_2, so it might be expected that it holds for a typical rational triangle billiard, and, conjecturally, for pseudo-integrable systems in general. The slopes of the fitted lines give an estimate of the compressibility as $\chi_\gamma = 1/p$. The values are given in Table II and compared with the other methods of estimation.

B. Two-point correlations

This section is devoted to the discussion of the results for the number variance and spectral form factors. Let us first examine the number variance. Figure 6 shows the number variance for each triangular billiard. The qualitative behavior is similar in all cases, and the number variance reaches a seemingly linear regime at $L \approx 10$. This corroborates with the expectations of intermediate-type statistics in rational billiards. The fit of straight lines permits to determine the slopes which determine the compressibility χ_{Σ^2}. The results

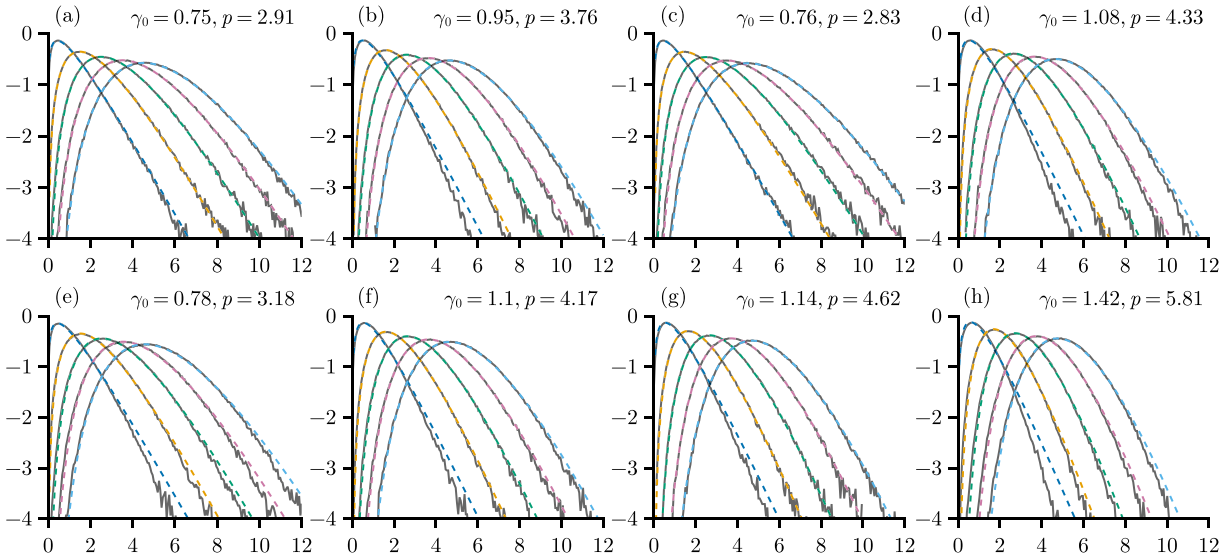

FIG. 5. Level spacing distributions in the decadic logarithmic scale $\log P_n(s)$ up to order $n = 4$, for all triangles considered in the study. The numerical data are shown in gray and the dashed colored curves show the gamma distributions (10) with parameters γ_n given by the linear relation (14). The linear parameters are obtained by fitting the line as shown in Fig. 3 and noted at the top right of each panel. The panels show the triangles (a) V_5, (b) V_7, (c) V_8, (d) V_9, (e) V_{10}, (f) V_{18}, (g) T_1, (h) T_2.

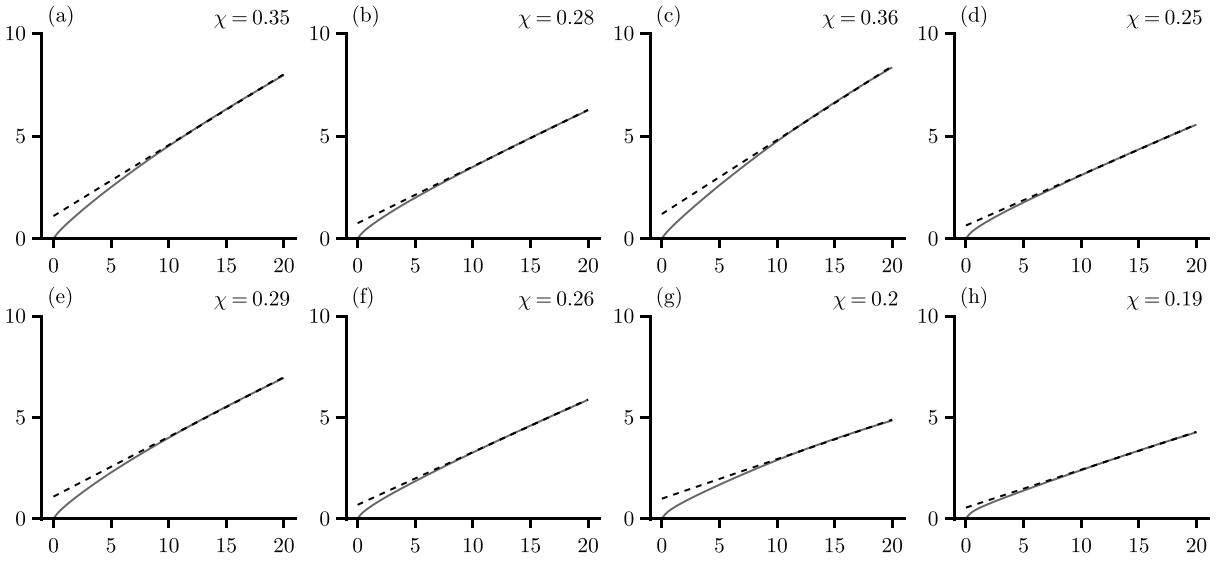

FIG. 6. The number variance $\Sigma^2(L)$ for all triangles considered in the study. The data are shown in gray. The black dashed line shows the slope that best fits the data, giving the compressibility χ. The sequence of triangles is the same as in Fig. 5.

are given in Table II. Since the spectra are finite, the number variance will eventually saturate and oscillate around the saturation plateau (see [62] and references therein). Because of this, it is not easy to extrapolate if the asymptotic regime has been reached. The extracted compressibilities are therefore less reliable and may be seen as only a rough estimate.

The connected spectral form factors (see discussion at the end of Sec. II) are plotted in Fig. 7. It is again evident that the spectral statistics are of the intermediate type as $K(t)$ approaches a finite value as $t \to 0$, in all triangles under consideration. The numerical results are compared to the analytical curves obtained by inserting the Laplace transform of the correlation function based on the gamma model (28) into Eq. (25). The function has two parameters p and γ_0 that are given by the slope and the intercept of the linear relation (14). In order to check the consistency of the model, the parameters to the numerical form factors are not fitted but instead the parameters obtained in fitting the level spacing distributions, given in Table II, are used. We see the analytical curves fit the data quite well, confirming that the parameters give consistent results. The insets show the small-t behavior, where we observe an oscillation resulting in a sudden drop, as $t \to 0$ in the numerical data. Very similar behavior was observed for generic right triangles in Ref. [22]. This is likely a consequence of the finite size of the spectral sample, as the sudden drop tends to move further towards 0 as the sample size is increased and can be considered a finite-size effect. Since the analytical curves are based on the same fitting parameters as the level spacing distributions, they imply the same values for the compressibility, namely, $\chi = 1/p$.

TABLE II. Model parameters and spectral compressibilities for all triangles. The linear gamma model parameters Eq. (14) are the intercept γ_0 and slope p. The compressibilites are obtained from the spectral form factor χ_K (coinciding with $\chi_\gamma = 1/p$; Fig. 7), the slope of the number variance χ_{Σ^2} (Fig. 6), and the semiclassical periodic orbit computation (only for the Veech triangles) (4).

Label	γ_0	p	χ_K	χ_{Σ^2}	χ_{PO}
V_5	0.75	2.15	0.46	0.35	0.55
V_7	0.95	2.81	0.36	0.28	0.47
V_8	0.76	2.07	0.48	0.36	0.55
V_9	1.08	3.25	0.31	0.25	0.43
V_{10}	0.78	2.40	0.42	0.29	0.50
V_{18}	1.10	3.07	0.33	0.26	0.50
T_1	1.14	3.48	0.29	0.20	N/A
T_2	1.42	4.39	0.23	0.19	N/A

The complete results for the compressibilities are gathered in Table II. We observe the values, extracted from the level spacings (equivalently spectral form factors) and the ones extracted from the number variances do not correspond exactly (generally $\chi_{\Sigma^2} < \chi_K$). However, they are approximately proportional when considering them as a property of each triangle. We expect further increasing the number of levels for the computation of the number variance, thereby allowing us to get closer to the asymptotic regime, would bring the two values closer together. Let us further compare the analytical results for the Veech triangles with the numerics. In general, we see the values from the numerics are slightly smaller than the analytical results. This is not entirely unexpected, since the analytical periodic orbit calculations take into account only the diagonal approximation [32] and higher orders in the asymptotic expansion and contributions from diffractive orbits are not analytically available. The triangles V_5 and V_7 consistently give similar values of the compressibility (and have similar spectral statistics in general), while the numerics show quite distinct spectral statistics for V_{10} and V_{18}.

IV. CONCLUSIONS AND DISCUSSION

The paper presents the detailed analysis of the spectral statistics of high excited energy levels of eight rational triangular quantum billiards belonging to the class of pseudo-integrable dynamical systems. The principal result is that the

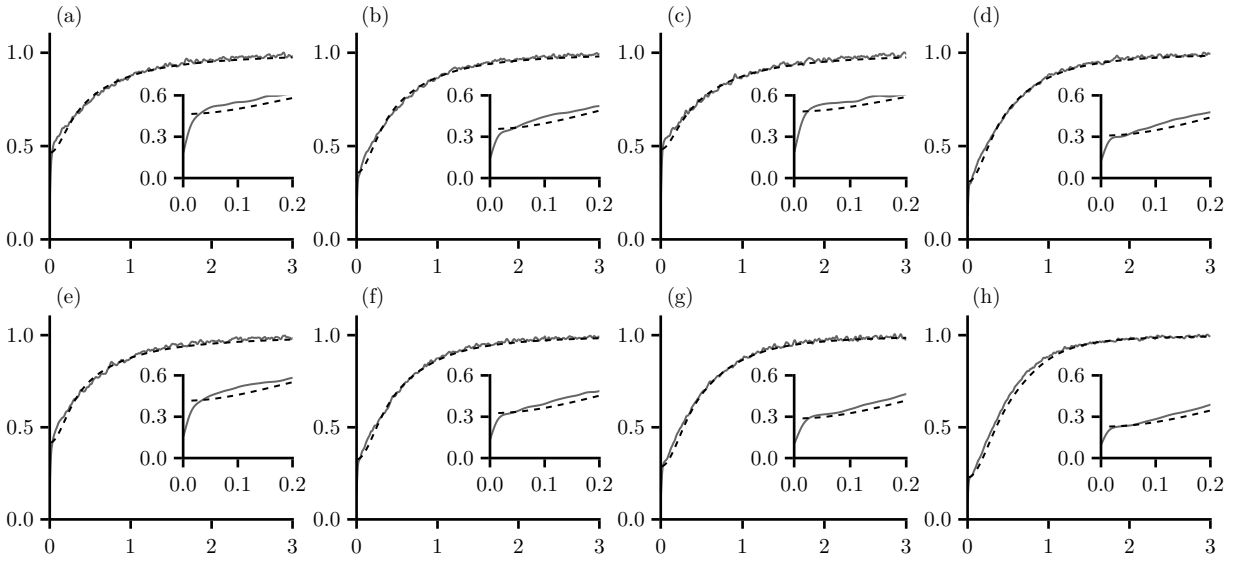

FIG. 7. Connected spectral form factors $K(t)$, for all triangles considered in the study. The data are shown in gray. The black dashed curve shows the model obtained by inserting the expression (28) into Eq. (25). The parameters p and γ_0 are the same as in Fig. 5. The sequence of triangles is the same as in Fig. 5.

level spacing statistics of such billiards are of the intermediate type and rather accurately described by the model of gamma distributions.

The characteristic features of observed statistics are the following: (1) The level spacing distributions exhibit level repulsion and have exponential tails. (2) The shape parameter of the higher order level spacings γ_n is linearly dependent on the order. (3) The level compressibility is nontrivial $0 < \chi < 1$, as seen in the linear regime of the number variance and the spectral form factor at the origin. and (4) The compressibility and proportionality coefficient of the level spacing shape parameter are approximately related by $\chi = 1/p$.

The normalized gamma distributions (12) provide a nearly perfect fit to the level spacing data. Thus, one can interpret them as a Wigner-type surmise that is a quite close approximation to the underlying analytically unknown probability distribution. The linear relation of the shape parameters and order of the level spacings (10) are consistent with previous results from structured random matrices and short-range plasma models [43]; however, the slope is not universal for all triangles. Since the level spacing distributions are easy to compute in contrast to the spectral form factors (or even the number variance) this provides an easily accessible way of determining the compressibility directly from the slope. The numerical results for the spectral form factor show a good agreement with the analytical expression (28) derived from the gamma distributions. The results for the more general obtuse triangles show that the special lattice property of the Veech triangles seems to be not essential for the applicability of the gamma model, which may indicate that it is relevant for general pseudo-integrable systems.

ACKNOWLEDGMENTS

We thank T. Prosen and B. Dietz for inspiring discussions, as well as the organizers of the 8th Dynamics Days Central Asia and Caucasus conference in Bukhara for facilitating the opportunity for the authors of this paper to meet in person. Č.L. thanks the Max Planck Society for its hospitality.

APPENDIX A: TOY MODEL

In this paper it has been observed that the simple gamma fit (12) describes the nth nearest-neighbor distributions for all considered triangular billiards quite well. The choice of such a fitting function is not based on profound theoretical grounds. It is just a simple function which tends to zero at small x to describe the level repulsion and has an exponential tail at large argument, which is a characteristic feature of the intermediate statistics. In addition, models exist where such a type of functions is exact [63].

To understand the accuracy of gamma fits, it is instructive to consider the following toy model. Let M be a 2×2 random symmetric matrix

$$M = \begin{pmatrix} e & v \\ v & -e \end{pmatrix}, \tag{A1}$$

where $e > 0$ and $v > 0$ are real random variables with probability densities $R(e)$ and $Q(v)$,

$$\int_0^\infty R(e)\,de = 1, \quad \int_0^\infty Q(v)\,dv = 1. \tag{A2}$$

Notice that the distributions are normalized over the interval $[0, \infty)$. When distributions are symmetric, this is a matter of convention.

The eigenvalues of this matrix are $\lambda_{1,2} = \pm\sqrt{e^2 + v^2}$, and the distribution of the spacing is

$$\begin{aligned} P(s) &= \int \delta(s - 2\sqrt{e^2 + v^2}) R(e) Q(v)\,de\,dv \\ &= \frac{s}{4} \int_0^{\pi/2} R[s\cos(\phi)/2] Q[s\sin(\phi)/2]\,d\phi. \end{aligned} \tag{A3}$$

When $R(e)$ and $Q(v)$ are the Gaussians with zero mean and equal variance, one gets the usual GOE Wigner surmise.

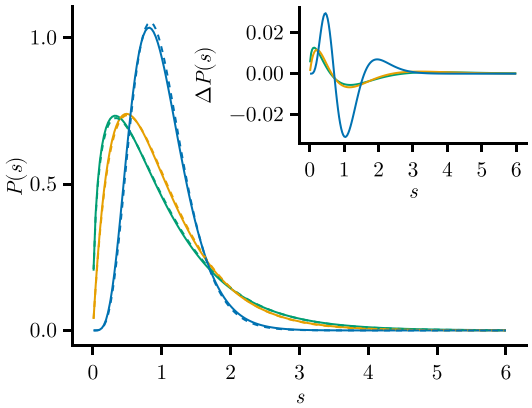

FIG. 8. Toy model distribution (A5) for different values of ν. Green line: $\nu = -1/2$, yellow line: $\nu = 0$, blue line: $\nu = 4$. Dashed lines of the same color indicate the gamma distribution (12) with $\gamma = 1/2,\ 1,\ 5$, respectively. All distributions are normalized on the unit first momentum. Insert: The differences between the toy model distributions and the corresponding gamma distributions.

Let us assume that $R(e)$ is the exponential function (to mimic the Poisson distribution) but off-diagonal variable v is distributed according to a gamma distribution $Q(v)$,

$$P(e) = \exp(-e), \qquad Q(v) = \frac{v^{\nu}}{\Gamma(\nu+1)}\exp(-v). \tag{A4}$$

After a rescaling, the spacing distribution in such a case is

$$P^{(\text{toy model})}(s) = \frac{\lambda^{\nu+2}s^{\nu+1}}{2^{\nu+2}\Gamma(\nu+1)}\int_0^{\pi/2}\sin^{\nu}(\phi) \times \exp\left(-\frac{\lambda s}{2}[\cos(\phi)+\sin(\phi)]\right)d\phi, \tag{A5}$$

where λ is fixed by the normalization of the first moment

$$(n+1)\lambda = \int_0^{\infty} ds \frac{s^{\nu+2}}{2^{\nu+2}\Gamma(\nu+1)}\int_0^{\pi/2}\sin^{\nu}(\phi)$$

$$\times \exp\left(-\frac{s}{2}[\cos(\phi)+\sin(\phi)]\right)d\phi = 2(\nu+2)(\nu+1)\int_0^{\pi/2}\frac{\sin^{\nu}(\phi)\,d\phi}{[\cos(\phi)+\sin(\phi)]^{\nu+3}}. \tag{A6}$$

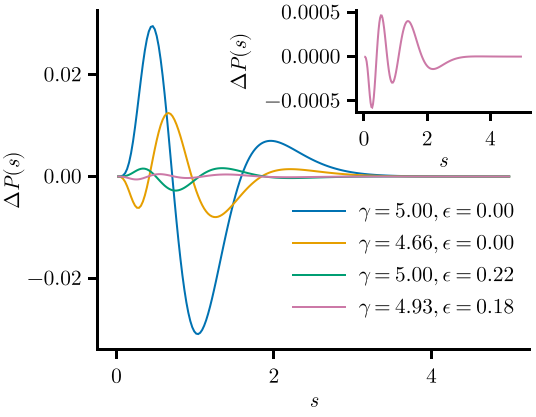

FIG. 9. Differences between toy model distribution (A5) with $\nu = 4$ and different fits $\Delta P(s) = P^{(\text{toy model})}(s) - P^{(\text{model})}(s)$. Blue line: gamma distribution with $\gamma = 5$; yellow line: gamma distribution with fitted $\gamma = 4.660$; green line: the first correction to the gamma distribution (A9) with $\gamma = 5$ and $\epsilon = 0.218$; magenta line: two-parameter fit of (A9) with $\gamma = 4.934$ and $\epsilon = 0.181$. Insert: The same magenta line as in the main figure but in a finer scale.

These integrals, in general, cannot be expressed in terms of known functions. In Fig. 8 this distribution computed numerically is plotted by solid color curves for three different values of $\nu = -1/2,\ 0,\ 4$. The dashed lines of the corresponding color indicate the gamma distributions (12) with $\gamma = \nu + 1$, i.e., which have the same power of s at small argument as $P^{(\text{toy model})}(s)$. It is clearly seen that these simple formulas are in a good agreement with numerical calculated distributions without any fits. For $\nu = 0$ this fact was mentioned in [64].

The gamma distributions are not exact and small deviations are, of course, present. In the insert of Fig. 8 the differences between $P^{(\text{toy model})}(s)$ and the indicated gamma distributions are plotted. For small ν the difference is of the order of 0.01 but for $\nu = 4$ it is around 0.03. To get a better approximation, it is natural to fit the parameter γ in (12) from the data and/or to propose another fitting distributions.

At Fig. 9 the differences between $P^{(\text{toy model})}(s)$ with $\nu = 4$ and different fits are shown. The blue line is the same as in the insert of Fig. 8 where the gamma distribution with $\gamma = 5$ was used. The yellow line corresponds to the gamma distribution (12) but with the fitted value of γ. It is the same procedure which used in the main text. The fit gives $\gamma \approx 4.66$. The use of a fitted γ roughly speaking reduces the discrepancy twice with respect to $\gamma = 5$. Though such simple approximation is enough for practical purposes, one may be interested in better estimations. The usual way of fitting unknown distributions consists in expanding them in a series of suitable functions. As the gamma distribution by itself is a good first approximation one can, e.g., use the following series:

$$P(s) = P^{(\text{gamma})}(s)\left(1 + \sum_{j=2}\epsilon_j p_j(s)\right), \tag{A7}$$

where ϵ_j are arbitrary constants and $p_j(s)$ are polynomials of order j orthogonal with respect to $P^{(\text{gamma})}(s)$:

$$\int_0^{\infty} P^{(\text{gamma})}(s)p_j(s)p_k(s)\,ds = h_j\delta_{jk}. \tag{A8}$$

For $P^{(\text{gamma})}(s)$ such polynomials are known as the generalized Laguerre polynomials (see, e.g., [65]). The sum starts with the polynomial of the second degree to get the imposed normalizations unchanged. The first correction term corresponds to the following expression:

$$P(s) = \frac{\lambda^{\gamma+1}}{\Gamma(\gamma+1)}s^{\gamma}e^{-\lambda s}\left\{1 + \epsilon\left[1 - \frac{2\lambda s}{\gamma+1} + \frac{\lambda^2 s^2}{(\gamma+2)(\gamma+1)}\right]\right\}. \tag{A9}$$

This function depends on two independent parameters γ and ϵ. In Fig. 9 the yellow line is the difference between the numerically computed toy model distribution with $\nu = 4$ and function (A9) with fixed $\gamma = 5$ and fitted ϵ. The one-

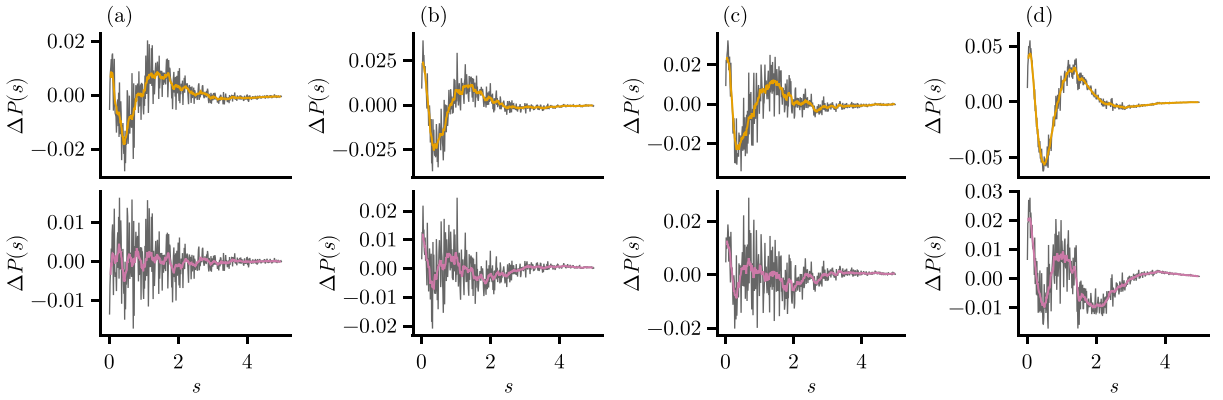

FIG. 10. Comparison of the differences of the nearest neighbor level spacing distributions $\Delta P(s) = P^{(\text{data})}(s) - P^{(\text{model})}(s)$ for several triangular billiards and the refined two-parameter gamma models using the correction given by Eq. (A9). The tow row shows just the best fitted gamma model without correction terms, setting $\epsilon = 0$, and the bottom row shows the correction with fitted ϵ. The data are taken from the spectra of triangles (a) V_{10}, (b) V_{18}, (c) T_1, (d) T_2. The colored lines show the averages over 10 points to more easily identify the trends in the data.

parameter fit gives $\epsilon \approx 0.218$. The amplitude of remaining deviations is smaller than 0.003. One can also fit the data by (A9) considered as a function of two fitted parameters γ and ϵ. The fit gives $\gamma = 4.934$ and $\epsilon = 0.181$. The difference from the toy model distribution with these two parameters fitted is indicated in Fig. 9 by the magenta line. This difference is so small (less than 0.0004) that it is almost invisible in the scale of the figure. The same difference but at much finer scale is shown in the insert of the same figure.

Of course, one could invent many different formulas to fit an unknown distribution. Beside many of them, a simple gamma fit gives a rather accurate approximation (in many cases less than 0.01) and has an additional advantage that all its moments can easily be calculated in a closed form. If necessary, higher order approximations can be used to find a more refined approximation.

APPENDIX B: TWO-PARAMETER FITS

It is plain that better approximations can also be developed for level distributions of triangular billiards. Consider, for example, the nearest-neighbor distributions for the right triangles with angles $\pi/10$ and $\pi/18$. In Fig. 10 the differences between numerical data and the gamma fits are presented in the top row [Figs. 10(a) and 10(b)]. Though the gamma fits give quite good results, small regular deviations (similar to the toy model) are clearly visible in these figures. The same may be seen for the two obtuse triangles [Figs. 10(c) and 10(d)]. The bottom row shows the two-parameter fit (A9) with fitted values of γ and ϵ. This helps to reduce the difference between the data. The same is true for the obtuse triangles presented in Figs. 10(c) and 10(d). The fit is especially good for the triangle V_{10} [see Fig. 10(a)] as it seems to be structureless and random.

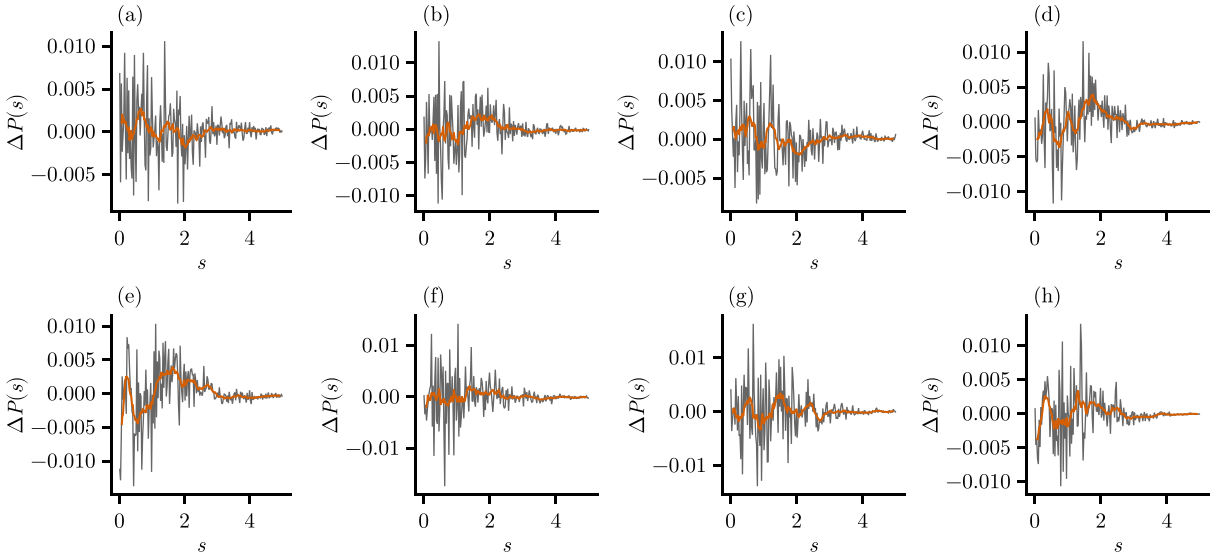

FIG. 11. Comparison of the differences of the nearest-neighbor level spacing distributions $\Delta P(s) = P^{(\text{data})}(s) - P^{(\text{Besselfit})}(s)$ for all triangular billiards and the two-parameter Bessel models using the correction given by Eq. (B1). The panels show the triangles (a) V_5, (b) V_7, (c) V_8, (d) V_9, (e) V_{10}, (f) V_{18}, (g) T_1, (h) T_2. The colored lines show the averages over 10 points to more easily identify the trends in the data.

TABLE III. Best fitting parameters for the expanded gamma model (A9) and Bessel fit (B1), fitted to the nearest-neighbor level spacing distributions of the triangular billiards.

Label	γ	ϵ	α	β
V_5	0.854	0.012	1.309	0.42
V_7	1.064	−0.057	1.825	0.892
V_8	0.848	0.029	1.243	0.289
V_9	1.147	−0.132	2.366	1.447
V_{10}	0.848	−0.069	1.64	0.903
V_{18}	1.131	−0.123	2.314	1.409
T_1	1.225	−0.121	2.4	1.416
T_2	1.300	−0.315	4.64	3.688

Let us consider, for diversity, a different kind of two-parameter fit,

$$P_n^{(\text{Bessel fit})}(s) = c\, q^{\alpha+1}\, s^{\alpha}\, K_\beta(qs), \tag{B1}$$

where $K_\beta(x)$ is the modified Bessel function of the third kind. Constants $c \equiv c(\alpha, \beta)$, and $q \equiv q(\alpha, \beta, n)$ are determined from the normalization conditions

$$c(\alpha, \beta) = \{2^{\alpha-1}\Gamma[(\alpha-\beta+1)/2]\Gamma[(\alpha+\beta+1)/2]\}^{-1}, \tag{B2}$$

$$q(\alpha, \beta, n) = \frac{2\Gamma[(\alpha-\beta)/2+1]\Gamma[(\alpha+\beta)/2+1]}{(n+1)\Gamma[(\alpha-\beta+1)/2]\Gamma[(\alpha+\beta+1)/2]}. \tag{B3}$$

This function has two independent parameters: α and β. Such a function but with $\beta = \alpha - 1$ has been proposed in [66] to approximate the nearest-neighbor distribution for a quantum limaçon billiard with mixed phase space.

Following the known asymptotic behaviors of $K_\beta(x)$, the Bessel fit (B1) has power asymptotics at small s and exponential at large s. But contrary to the gamma fit, the powers at small and large s may be different. For half-integer β, $K_\beta(x)$ is expressed through elementary functions. In particular, for $\beta = 1/2$ the Bessel fit coincides with the gamma fit. In Fig. 11 the difference between the nearest-neighbor level spacing distributions for all triangles and the Bessel fits is shown. The resulting oscillations are small and in some cases appear purely random. As expected, two-parameter fits give better approximations but are more complicated and less transparent. The best fitting parameters are presented in Table III.

[1] H.-J. Stöckmann, *Quantum Chaos—An Introduction* (Cambridge University Press, Cambridge, 1999).

[2] F. Haake, *Quantum Signatures of Chaos* (Springer, Berlin, 2001).

[3] G. Casati, F. Valz-Gris, and I. Guarneri, On the connection between quantization of nonintegrable systems and statistical theory of spectra, Lett. Nuovo Cimento **28**, 279 (1980).

[4] O. Bohigas, M. J. Giannoni, and C. Schmit, Characterization of chaotic quantum spectra and universality of level fluctuation laws, Phys. Rev. Lett. **52**, 1 (1984).

[5] M. V. Berry, Regular and irregular semiclassical wavefunctions, J. Phys. A: Math. Gen. **10**, 2083 (1977).

[6] P. J. Richens and M. V. Berry, Pseudointegrable systems in classical and quantum mechanics, Physica D **2**, 495 (1981).

[7] A. N. Zemlyakov and A. B. Katok, Topological transitivity in billiards in polygons, Math. Notes **18**, 760 (1975).

[8] E. Gutkin, Billiards in polygons, Physica D **19**, 311 (1986).

[9] E. Gutkin, Billiards in polygons: Survey of recent results, J. Stat. Phys. **83**, 7 (1996).

[10] Y. G. Sinai, On the foundations of the ergodic hypothesis for a dynamical system of statistical mechanics, Sov. Math. Dokl. **4**, 1818 (1963).

[11] L. A. Bunimovich, On billiards close to dispersing, Math. USSR Sbornik **23**, 45 (1974).

[12] L. A. Bunimovich, On the ergodic properties of nowhere dispersing billiards, Commun. Math. Phys. **65**, 295 (1979).

[13] R. E. Schwartz, Obtuse triangular billiards II: One hundred degrees worth of periodic trajectories, Exp. Math. **18**, 137 (2009).

[14] W. A. Veech, Teichmüller curves in moduli space, Eisenstein series and an application to triangular billiards. Invent. Math. **97**, 553 (1989).

[15] G. Casati and T. Prosen, Mixing property of triangular billiards, Phys. Rev. Lett. **83**, 4729 (1999).

[16] R. Artuso, G. Casati, and I. Guarneri, Numerical study on ergodic properties of triangular billiards, Phys. Rev. E **55**, 6384 (1997).

[17] J. Wang, G. Casati, and T. Prosen, Nonergodicity and localization of invariant measure for two colliding masses, Phys. Rev. E **89**, 042918 (2014).

[18] J. Huang and H. Zhao, Ultraslow diffusion and weak ergodicity breaking in right triangular billiards, Phys. Rev. E **95**, 032209 (2017).

[19] K. Zahradova, Ergodic properties of triangular billiards: A numerical study, Ph.D. thesis, Queen Mary University of London, 2022.

[20] K. Zahradova, J. Slipantschuk, O. F. Bandtlow, and W. Just, Impact of symmetry on ergodic properties of triangular billiards, Phys. Rev. E **105**, L012201 (2022).

[21] K. Zahradova, J. Slipantschuk, O. F. Bandtlow, and W. Just, Anomalous dynamics in symmetric triangular irrational billiards, Physica D **445**, 133619 (2023).

[22] Č. Lozej, G. Casati, and T. Prosen, Quantum chaos in triangular billiards, Phys. Rev. Res. **4**, 013138 (2022).

[23] W. P. Hooper, Another Veech triangle, Proc. Am. Math. Soc. **141**, 857 (2013).

[24] T. Cheon and T. D. Cohen, Quantum level statistics of pseudointegrable billiards, Phys. Rev. Lett. **62**, 2769 (1989).

[25] A. Shudo and Y. Shimizu, Extensive numerical study of spectral statistics for rational and irrational polygonal billiards, Phys. Rev. E **47**, 54 (1993).

[26] A. Shudo, Y. Shimizu, P. Šeba, J. Stein, H. Stöckmann, and K. Życzkowski, Statistical properties of spectra of pseudointegrable systems, Phys. Rev. E **49**, 3748 (1994).

[27] H. C. Schachner and G. M. Obermair, Quantum billiards in the shape of right triangles, Z. Phys. B **95**, 113 (1994).

[28] E. B. Bogomolny, U. Gerland, and C. Schmit, Models of intermediate spectral statistics, Phys. Rev. E **59**, R1315 (1999).

[29] B. Grémaud and S. R. Jain, Spacing distributions for rhombus billiards, J. Phys. A: Math. Gen. **31**, L637 (1998).

[30] J. Wiersig, Spectral properties of quantized barrier billiards, Phys. Rev. E **65**, 046217 (2002).

[31] M. V. Berry, Semiclassical theory of spectral rigidity, Proc. R. Soc. London A: Math. Phys. Sci. **400**, 229 (1985).

[32] E. Bogomolny, O. Giraud, and C. Schmit, Periodic orbits contribution to the 2-point correlation form factor for pseudointegrable systems, Commun. Math. Phys. **222**, 327 (2001).

[33] E. Bogomolny, Barrier billiard and random matrices, J. Phys. A: Math. Theor. **55**, 024001 (2022).

[34] E. Bogomolny, Random matrices associated with general barrier billiards, J. Phys. A: Math. Theor. **55**, 254002 (2022).

[35] E. Bogomolny and C. Schmit, Structure of wave functions of pseudointegrable billiards, Phys. Rev. Lett. **92**, 244102 (2004).

[36] E. Bogomolny, Formation of superscar waves in plane polygonal billiards, J. Phys. Commun. **5**, 055010 (2021).

[37] B. L. Altshuler, I. K. Zharekeshev, S. Kotochigova, and B. Shklovskii, Repulsion between energy levels and the metal-insulator transition, J. Exp. Theor. Phys **67**, 625 (1988).

[38] B. I. Shklovskii, B. Shapiro, B. R. Sears, P. Lambrianides, and H. B. Shore, Statistics of spectra of disordered systems near the metal-insulator transition, Phys. Rev. B **47**, 11487 (1993).

[39] B. Dietz, Semi-Poisson statistics in relativistic quantum billiards with shapes of rectangles, Entropy **25**, 762 (2023).

[40] O. Giraud, J. Marklof, and S. O'Keefe, Intermediate statistics in quantum maps, J. Phys. A: Math. Gen. **37**, L303 (2004).

[41] E. Bogomolny, U. Gerland, and C. Schmit, Short-range plasma model for intermediate spectral statistics, Eur. Phys. J. B **19**, 121 (2001).

[42] E. Bogomolny, Spectral statistics of random Toeplitz matrices, Phys. Rev. E **102**, 040101(R) (2020).

[43] E. Bogomolny and O. Giraud, Statistical properties of structured random matrices, Phys. Rev. E **103**, 042213 (2021).

[44] E. G. Vergini and M. Saraceno, Calculation by scaling of highly excited states of billiards, Phys. Rev. E **52**, 2204 (1995).

[45] E. G. Vergini, Estudio cuantico y semiclasico de billares clasicamente caoticos, Ph.D. thesis, Universidad de Buenos Aires, 1995.

[46] A. H. Barnett, Dissipation in deforming chaotic billiards, Ph.D. thesis, Harvard University, 2001.

[47] A. H. Barnett and T. Betcke, Quantum mushroom billiards, Chaos **17**, 043125 (2007).

[48] Č. Lozej, B. Batistić, and D. Lukman, Quantum billiards, https://github.com/clozej/quantum-billiards/tree/crt_public.

[49] H. P. Baltes and E. R. Hilf, *Spectra of Finite Systems* (BI-Wissenschaftsverlag, Mannheim, 1976).

[50] M. V. Berry and M. Tabor, Level clustering in the regular spectrum, Proc. R. Soc. London A: Math. Phys. Sci. **356**, 375 (1977).

[51] W.-J. Rao, Higher-order level spacings in random matrix theory based on Wigner's conjecture, Phys. Rev. B **102**, 054202 (2020).

[52] F. M. Izrailev, Simple models of quantum chaos: Spectrum and eigenfunctions, Phys. Rep. **196**, 299 (1990).

[53] B. Batistić and M. Robnik, Dynamical localization of chaotic eigenstates in the mixed-type systems: Spectral statistics in a billiard system after separation of regular and chaotic eigenstates, J. Phys. A: Math. Theor. **46**, 315102 (2013).

[54] B. Batistić, Č. Lozej, and M. Robnik, The level repulsion exponent of localized chaotic eigenstates as a function of the classical transport time scales in the stadium billiard, Nonlinear Phenom. Complex Syst. **21**, 225 (2018).

[55] Č. Lozej, Spectral form factor and dynamical localization, Entropy **25**, 451 (2023).

[56] T. A. Brody, A statistical measure for the repulsion of energy levels, Lett. Nuovo Cimento **7**, 482 (1973).

[57] M. L. Mehta, *Random Matrices* (Academic Press, Boston, 2004).

[58] R. E. Prange, The spectral form factor is not self-averaging, Phys. Rev. Lett. **78**, 2280 (1997).

[59] A. Delon, R. Jost, and M. Lombardi, NO_2 jet cooled visible excitation spectrum: Vibronic chaos induced by the $\tilde{X}\ ^2A_1 - \tilde{A}\ ^2B_2$ interaction, J. Chem. Phys. **95**, 5701 (1991).

[60] H. Alt, H.-D. Gräf, T. Guhr, H. L. Harney, R. Hofferbert, H. Rehfeld, A. Richter, and P. Schardt, Correlation-hole method for the spectra of superconducting microwave billiards, Phys. Rev. E **55**, 6674 (1997).

[61] M. Winer and B. Swingle, Hydrodynamic theory of the connected spectral form factor, Phys. Rev. X **12**, 021009 (2022).

[62] A. Bäcker, F. Steiner, and P. Stifter, Spectral statistics in the quantized cardioid billiard, Phys. Rev. E **52**, 2463 (1995).

[63] E. Bogomolny and C. Schmit, Spectral statistics of a quantum interval-exchange map, Phys. Rev. Lett. **93**, 254102 (2004).

[64] L. Kong, Z. Gong, and B. Wu, Quantum dynamical tunneling breaks classical conserved quantities, Phys. Rev. E **109**, 054113 (2024).

[65] H. Bateman and A. Erdélyi, *Higher Transcendental Functions*, Bateman Manuscript Project (McGraw-Hill, New York, 1953), Vol. II.

[66] I. R. R. González, A. M. S. Macêdo, G. L. Vasconcelos, and E. P. Raposo, Unified stochastic formalism for the regular-to-chaotic transition in quantum billiards (unpublished).